HEALTH AND MEDICINE

Platelet-derived porous nanomotor for thrombus therapy

Mimi Wan[1]*†, Qi Wang[1,2]*, Rongliang Wang[3], Rui Wu[3], Ting Li[1], Dan Fang[1], Yangyang Huang[1], Yueqi Yu[1], Leyi Fang[1], Xingwen Wang[1], Yinghua Zhang[1], Zhuoyue Miao[1], Bo Zhao[1], Fenghe Wang[2], Chun Mao[1]†, Qing Jiang[3], Xingquan Xu[3], Dongquan Shi[3]†

The treatment difficulties of venous thrombosis include short half-life, low utilization, and poor penetration of drugs at thrombus site. Here, we develop one kind of mesoporous/macroporous silica/platinum nanomotors with platelet membrane (PM) modification (MMNM/PM) for sequentially targeting delivery of thrombolytic and anticoagulant drugs for thrombus treatment. Regulated by the special proteins on PM, the nanomotors target the thrombus site and then PM can be ruptured under near-infrared (NIR) irradiation to achieve desirable sequential drug release, including rapid release of thrombolytic urokinase (3 hours) and slow release of anticoagulant heparin (>20 days). Meantime, the motion ability of nanomotors under NIR irradiation can effectively promote them to penetrate deeply in thrombus site to enhance retention ratio. The in vitro and in vivo evaluation results confirm that the synergistic effect of targeting ability from PM and motion ability from nanomotors can notably enhance the thrombolysis effect in both static/dynamic thrombus and rat model.

INTRODUCTION

Venous thrombosis, including deep vein thrombosis and pulmonary embolism, has a high incidence worldwide, with an annual incidence of about 1 to 3 per mil, which is potentially life-threatening (*1*–*3*). At present, the treatment of venous thrombosis mainly contains two stages. In the early stage, thrombolytic drugs are used to recanalize veins, and in the later stage, anticoagulant drugs are used to prevent thrombosis regeneration (*4*, *5*). However, current therapy methods have some disadvantages. For example, because of the short half-life of thrombolytic drug (usually only a few minutes), frequent high-dose systemic administration is needed, which not only increases medical cost but also causes side effects such as bleeding, body allergy, and blood pressure instability (*6*, *7*). Meantime, pure drug injection also has the defect of low drug utilization rate due to the lack of targeting, that is, less than 5% of the drug reach the patient site (*8*, *9*). In addition, the thrombolytic drugs only remain on the thrombus surface, and it is difficult to penetrate into the embolus, which cannot obtain ideal therapeutic effect.

The development of self-driven nanomotors offers a possibility to solve the above problems. However, most of the nanomotors reported at present have some difficulties to overcome when applying them to treat thrombus. One important kind of nanomotors is to use metal to catalyze hydrogen peroxide (H_2O_2) to generate O_2 as the driving force. For instance, the catalytic material such as Pt is usually modified to mesoporous silica (MS)–based particles, which triggers the decomposition of H_2O_2 (*10*). Another important kind of nanomotors is to construct Janus nanomotors by vacuum sputtering of metals such as Au layer onto one side of the MS nanoparticles (NPs) (*11*). The movement ability of the former is based on the toxic fuel H_2O_2, which makes it impossible to apply it to the blood environment. The latter only uses ordinary MS with a single kind of mesoporous channel as carrier and has limited loading of drugs and types. Meantime, the metal loading method is surface sputtering, which is difficult to guarantee the stability of the combination of metal and the carrier.

When referring to the application of nanomotors in thrombolysis, many researchers report the construction of erythrocyte membrane–cloaked Janus polymeric micromotors propelled by near-infrared (NIR) irradiation and applied in thrombus ablation (*12*). The thrombolytic effect was achieved by using heparin (Hep) and photothermal effects. This is a beneficial attempt to apply nanomotors to thrombolysis. Yet, only some qualitative experiments were performed without specific thrombolytic effects such as using static and dynamic thrombolytic models. Evaluation of thrombolytic effect in vivo has not been involved, either. Meantime, many researchers also proposed that the recurrence risk after treatment is about 5 to 10% in the first 12 months (*13*, *14*). For thrombosis, a special disease, simple thrombolysis strategy cannot meet its needs, and the clinically preferred treatment method is a combination of short-term thrombolysis and long-term anticoagulation, thereby avoiding the regeneration of thrombus. This requirement usually means that drugs with different functions need to be loaded, and currently, there are no such nanomotors capable of accomplishing the above purposes at the same time.

Taking into account the problems of the current nanomotors mentioned above and the actual demand for disease treatment, NIR driving method was adopted to avoid the use of toxic fuels. To solve the problem that most porous nanomotor channels are difficult to load with different types of drugs, we use the "epitaxial growth" method to construct a mesoporous/macroporous composite structure at the same time. Moreover, an in situ reduction method was used to introduce Pt NPs into the macroporous structure to improve the metal bonding stability, and a proper confinement of the macroporous channels was used to fix the Pt NPs at 20 to 40 nm for improving their stability. Therefore, a kind of

[1]National and Local Joint Engineering Research Center of Biomedical Functional Materials, School of Chemistry and Materials Science, Nanjing Normal University, Nanjing 210023, China. [2]Jiangsu Province Key Laboratory of Environmental Engineering, School of Environment, Nanjing Normal University, Nanjing 210023, China. [3]Department of Sports Medicine and Adult Reconstructive Surgery, Nanjing Drum Tower Hospital, The Affiliated Hospital of Nanjing University Medical School, Nanjing 210008, China.
*These authors contributed equally to this work.
†Corresponding author. Email: wanmimi@njnu.edu.cn (M.W.); maochun@njnu.edu.cn (C.M.); shidongquan1215@163.com (D.S.)

mesoporous/macroporous silica (MMS)/platinum (Pt) nanomotors (MMNM) coated with platelet membrane (PM) (called MMNM/PM) was designed and prepared. The macroporous structure from the nanomotors can be loaded with large-sized thrombolytic drug of urokinase (UK; about 2 nm in width and 30 nm in length (*15*), while the mesoporous structure can be loaded with an anticoagulant drug of Hep (about 1 nm in width of and several nanometers in length) (*16*). As shown in Fig. 1, the nanomotors would go through the following stages after entering the blood environment: thrombus target, thrombus deep penetration, and vascular penetration. In the first stage, PM modification was a biomimetic method using the ability of platelets based on the abundant GPIIb/IIIa complex on the PM, realizing the effective aggregation of PM-modified nanomotors in thrombus sites (*17*–*19*). In the following stage, nonuniform distribution of Pt NPs in the MMNM/PM nanomotors can absorb NIR light and produce inhomogeneous heat distribution. Thereby, the nanomotors can be driven through thermophoresis (*11*, *20*). Thus, the MMNM/PM nanomotors that stayed on the thrombus surface can move into the thrombus under the irradiation of NIR light, thus increasing the penetration depth and retention ratio of MMNM/PM nanomotors at the thrombus site. At this stage, the existence of PM can also regulate the drug release process, which can be heated to rupture under NIR irradiation and the drugs can be released to a large content from the nanomotors, effectively avoiding the side effects of drugs reaching other parts of the body in the course of blood circulation (*21*). Meantime, the delayed drug release rate by PM can avoid the ineffective waste and corresponding side effects of drugs during the transport process. The nanomotors penetrated into blood vessels can stay there for long-term release of anticoagulant drug. This particular design can meet the need of thrombolysis therapy, in which more thrombolytic drugs were needed to dissolve thrombus in the early stage of treatment, and anticoagulant drugs were needed to prevent thrombus recurrence in long-term treatment, which had not been reported yet.

RESULTS

Characterizations of the nanomotors

The porous structure of the as-prepared MMNM was observed and proved by transmission electron microscope (TEM), scanning electron microscope, and N_2 adsorption-desorption isotherms. As shown in Fig. 2A, TEM images of MS core displayed a uniform particle size of about 100 nm and ordered mesoporous structure. TEM images of MMS with the particle size of about 390 nm showed an obvious fluffy macroporous layer (Fig. 2B). N_2 adsorption-desorption results further verified the ordered mesoporous structure in MS with mesoporous pore size of about 3.59 nm (fig. S1 and table S1). Meantime, the existence of macroporous structure can also be proved by the pore size distribution profiles of MMS and MMNM samples, which displays that the pore sizes were about 58.0 and 40.0 nm (figs. S2 and S3 and table S1). Further, TEM images of MMNM displayed that Pt NPs with a particle size of about 20 to 40 nm unevenly distributed in the macroporous structure (Fig. 2C). The successful encapsulation of PM at the outer layer of MMNM can be proved by Fig. 2D; the size changed from around 390 nm (MMNM) to about 410 nm (MMNM/PM). High-angle annular dark-field (HAADF) image (Fig. 2E) displayed that the morphology of MMNM/PM was similar with that of MMNM with obvious distribution of Pt NPs (red arrows), indicating the successful construction of MMNM/PM nanomotors. Furthermore, the TEM-mapping images (Fig. 2, F to L) were also obtained to confirm the existence of PM, which displays even distribution of P and S elements from PM. Moreover, an energy-dispersive spectrometer (EDS) of MMNM showed that the elemental amount ratio of Pt was about 4.8% (fig. S4).

Meantime, the presence of PM on the surface of MMNM/PM nanomotors can also be verified by their fluorescent images. Dual-fluorescence labeling of MMNM core and PM was conducted by staining MMNM with Cy5.5 (red), PM with DiO (green), and then confocal laser scanning microscopy (CLSM) was used to observe the fluorescence colocalization. Figure S5 displayed that red and green fluorescence overlapped perfectly for the MMNM/PM sample, implying

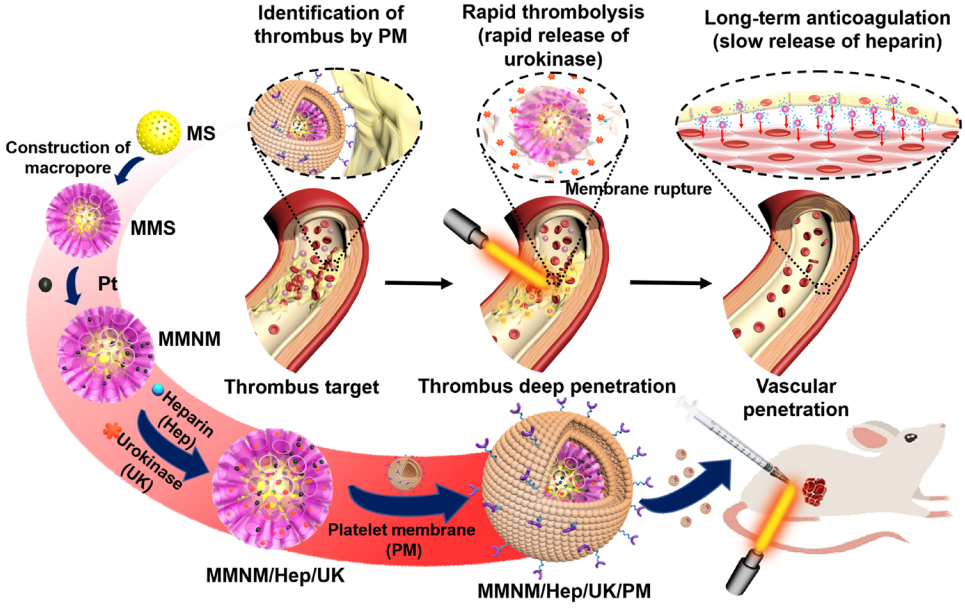

Fig. 1. Schematic illustration of the fabrication of MMNM/Hep/UK/PM nanomotors and their application for thrombus targeting and thrombolytic treatment.

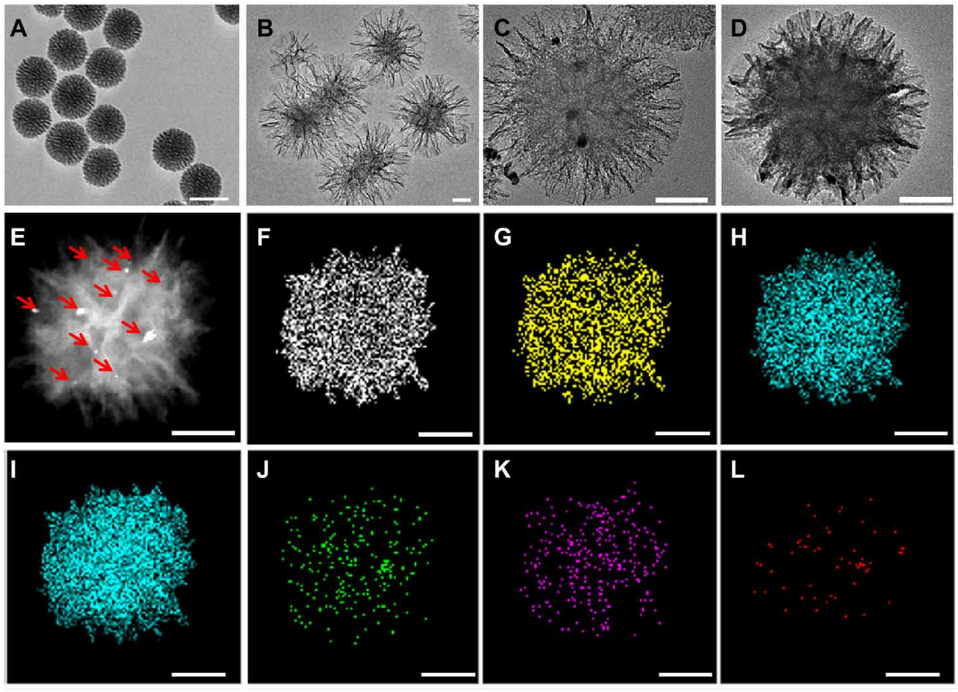

Fig. 2. Characterization of nanomotors. TEM images of (**A**) MS, (**B**) MMS, (**C**) MMNM, and (**D**) MMNM/PM; HAADF image of (**E**) MMNM/PM; and the corresponding TEM-mapping images of (**F**) C, (**G**) N, (**H**) O, (**I**) Si, (**J**) P, (**K**) S, and (**L**) Pt (scale bar, 100 nm).

that PM was wrapped outside MMNM. Thermal gravimetric (TG) measurement was used to determine the mass ratio of PM decorated on MMNM. It can be seen clearly from fig. S6 that the mass ratio of PM on MMNM was about 8.5% (the water content from MMNM/PM was removed by a vacuum freeze-drying process before TG measurement). Furthermore, zeta potential results also proved the successful coating of the negative charged PM outside the nanomotors (fig. S7) (*22*, *23*), as the surface charge changed from positive (+30.5 mV) for the amine-modified MMNM to negative (−12.2 mV) for the MMNM/PM nanomotors. Moreover, the existence of GpIIb/IIIa complex from PM and MMNM/PM were confirmed by Western blot (fig. S8), which displayed that the components of GpIIb/IIIa complex such as GpIIb and GpIIIa were expressed on both PM and MMNM/PM. Further, the NIR-triggered PM disruption was examined by using TEM, CLSM, and zeta potential characterization methods. CLSM images of MMNM/PM under NIR irradiation for 10 min (fig. S5) displayed that almost no green fluorescence (PM) can be observed and only red fluorescence can be seen. It can also be seen from fig. S9 that the TEM image of MMNM/PM-NIR displays similar morphology with that of MMNM. In addition, the zeta potential changes from negative (−12.2 mV) to positive (+6.8 mV) after NIR irradiation owing to the PM rupture caused by irradiation.

Furthermore, the motion behavior of the MMNM/PM nanomotors under NIR irradiation condition (808 nm) (movie S1) was studied. Because of the phenomenon of thermophoresis caused by the resonance absorption of asymmetric Pt NPs located in the macroporous structure under NIR irradiation, the nanomotors can be driven by asymmetric thermophoresis (*11*). The motion speeds of the MMNM/PM nanomotors increase with the increasing power densities (Fig. 3, A and B). Meantime, the motion behavior of the nanomotors under NIR irradiation was investigated by analyzing the mean squared displacement (MSD) during the motion process. The average value of MSD as a function of time can be calculated fitted to linear and parabola relationship (Fig. 3C, fig. S10, and tables S2 and S3), which showed that the motion of nanomotors can conform to the parabolic trend when the power densities were 1.5 and 2 W cm^{-2}, with the coefficient of determination (R^2) of 0.9934 and 0.9952, respectively. The above results implied that the motion of the nanomotor can be considered to be caused by the diffusion of particle self-propulsion under these conditions. For nanomotors under lower power densities, the MSD can be fitted to the more general form, MSD = $a \times t^{\alpha}$, in which α represented subdiffusion for $0 < \alpha < 1$ and superdiffusion for $1 < \alpha < 2$ (*24*). The α values for the fitted MSD plots of nanomotors under lower power densities (0.5 and 1 W cm^{-2}) were 1.49 and 1.05, respectively (fig. S10 and table S4), which indicated that the motion mode of the nanomotors was mainly subdiffusion at these conditions.

Analysis of drug loading and release behavior

The drug loading process was characterized by N_2 adsorption-desorption isotherms, TEM, dynamic light scattering (DLS), Fourier transform infrared (FTIR), and EDS characterizations (figs. S11 to S17). It can be seen from fig. S11 and table S1 that the specific surface area of the MMNM/Hep sample loaded with Hep dropped to 170.9 m^2 g^{-1}, and the mesoporous pore size was reduced. The reason for the decrease in specific surface area may be that Hep was mainly loaded in mesoporous channels, most of the Hep in MMNM macropores can be removed by the washing process, so MMNM/Hep still retained a certain specific surface area (170.9 m^2 g^{-1}). For MMNM/Hep/UK loaded with two drugs, the specific surface area was about 10.2 m^2 g^{-1}, which may be because both the mesoporous and macroporous structures were occupied by the drugs, so the exposed specific surface area was very low. For the MMNM/Hep/UK/PM sample loaded with the two drugs, the specific surface area was reduced to

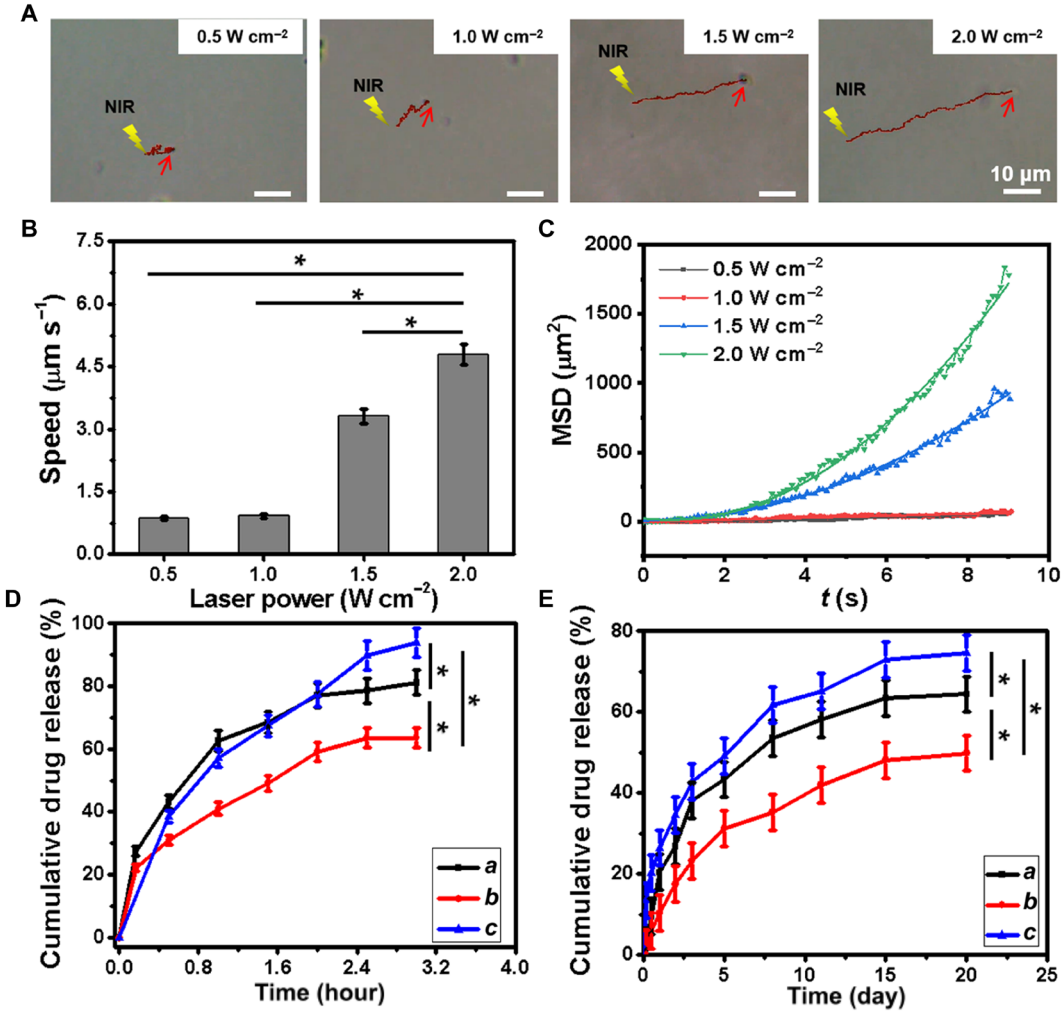

Fig. 3. Motion and drug release behavior of the nanomotors under different conditions. (**A**) Time-lapse images displaying the tracking trajectories, (**B**) speeds of MMNM/PM nanomotor under different NIR power densities (9 s), and (**C**) their corresponding parabolic fitting for MSD plots ($y = ax^2 + bx + c$) (movie S1). (**D**) UK and (**E**) Hep release profiles in vitro under different conditions (a, MMNM/Hep/UK; b, MMNM/Hep/UK/PM; c, MMNM/Hep/UK/PM + NIR). An asterisk denotes statistical significance between bars (*$P < 0.05$) using one-way analysis of variance (ANOVA). Experimental data are means ± SD of samples in a representative experiment ($n = 3$).

9.4 $m^2 g^{-1}$. TEM images of nanomotors with drugs were shown in fig. S12, which displayed that the mesoporous/macroporous structure of the nanomotors was maintained during the drug loading process. EDS spectra of nanomotor with drugs were evaluated to characterize the main composition of the samples with drugs. It can be seen from fig. S13 that Si and Pt existed in the MMNM sample, while the EDS spectrum of MMNM/Hep showed the existence of N and S, which can be ascribed to the existence of Hep (*25*). For MMNM/Hep/UK with two kinds of drugs, the EDS spectrum displayed the existence of both S and Br, implying the successful loading of Hep and UK in the samples [the molecular formula of UK: $(C_{21}H_{25}BrN_2O_3)_n$; bought from Aladdin]. DLS was used to evaluate the size change of particles during the drug loading process. It can be seen from fig. S14 that the hydrodynamic diameter of MMNM was about 389.6 nm, which was slightly larger than that obtained from TEM images. After loading of Hep, the hydrodynamic diameter of MMNM/Hep changes a little, indicating that Hep was loaded at the inner core of MMNM, which displayed little effect on the size of MMNM/Hep. In contrast, the hydrodynamic diameter of MMNM/Hep/UK increased a lot, probably owing to the fact that protein UK locates at the outer macropores, thus enhancing the hydrodynamic size of the sample. Furthermore, the rapture of PM under NIR irradiation can be confirmed by fig. S14 that the hydrodynamic diameter of MMNM/Hep/UK/PM decreased to about 458.7 nm after being irradiated by NIR light for 10 min. The FTIR spectra of the samples after the drug loading process were also obtained to characterize the structure of samples with drugs (figs. S15 to S17). Comparing the FTIR spectra of MMNM, Hep, and MMNM/Hep, we found that the FTIR spectrum of MMNM/Hep contained the characteristic peaks of MMNM and Hep, indicating that Hep was successfully loaded into the nanomotors. For MMNM/Hep/UK loaded with two drugs, the FTIR spectrum contained all the characteristic peaks of UK, Hep, and MMNM, among which the peak intensity around 1080 cm^{-1} increased; it was possible caused by the overlap of functional groups (—SO_3— and —COC—) of Hep and UK (*26*).

To investigate the sequential release behavior of UK and Hep from MMNM/Hep/UK/PM, MMNM/UK, and MMNM/Hep containing single drug, and MMNM/Hep/UK with two drugs were also prepared,

respectively. As shown in fig. S18, the release of UK from MMNM/UK can last for about 3 hours, which may be attributed to the fact that UK mostly located in the outer macropores of the nanomotors, while MMNM/Hep displayed a much slower release rate and the release of Hep can last for at least 20 days. Three classical release models were chosen to further reveal the release mechanism of UK and Hep [Zero-order ($Q_t = K_0t$), First-order ($\ln(1 - Q_t/Q_f) = -K_1t$), and Peppas ($M_t/M_\infty = a \cdot t^b$ or $\ln(M_t/M_\infty) = \ln a + b\ln t$), where Q_f is the total release amount of drugs and Q_t is the release amount of drugs at the time of t; K represents the rate constant of each release model; M_t represents the release amount of drugs at the time of t and M_∞ is the total release amount, while a is the kinetic constant and b is regarded as the exponent to identify the diffusion mechanism] (*27*). As shown in fig. S18 and table S5, the release performance of UK from MMNM/UK was best consistent with the Peppas model, indicating that the locations of UK were porous structures. The release of Hep from MMNM/Hep was more in line with the first-order model, suggesting that Hep from MMNM/Hep was released from multiple channels.

For MMNM/Hep/UK/PM nanomotors, the release of UK was almost saturated in 3 hours (Fig. 3D). It is worth noting that the cumulative release ratio of UK (81.2%) from MMNM/Hep/UK was higher than that of MMNM/Hep/UK/PM (63.6%), indicating that the outer PM may have a barrier effect on the drug release behavior of the nanomotor (*28*). Moreover, after being exposed to the NIR irradiation, the cumulative release ratio of UK from MMNM/Hep/UK/PM increased to 93.9%. One possible explanation for this phenomenon is that the temperature rise caused by NIR irradiation leads to the rupture of PM and motion ability of MMNM/Hep/UK/PM nanomotors driven by NIR irradiation can also enhance drug diffusion, increasing the cumulative release of drugs. As shown in Fig. 3E, a much slower release rate of Hep was observed on MMNM/Hep/UK/PM, indicating that the inner mesoporous structure can realize the delayed release of Hep. Then, the release mechanism of two drugs in MMNM/Hep/UK/PM nanomotors under NIR irradiation was also investigated. As shown in figs. S19 and S20 and table S6, UK ($R^2 = 0.9943$) and Hep ($R^2 = 0.9939$) released from MMNM/Hep/UK/PM nanomotor under NIR irradiation were more consistent with the Peppas model.

In vitro anticoagulability of the nanomotors

The in vitro anticoagulation and blood compatibility of different samples were then detected (fig. S21). MMNM with single drug (UK or Hep) and two drugs (UK and Hep) were also prepared for comparison. The activated partial thromboplastin time (APTT)/prothrombin time (PT)/thrombin time (TT) values of the blank and MMNM/UK were between 8.9 and 16.1 s, while MMNM/Hep, MMNM/Hep/UK, and MMNM/Hep/UK/PM display much higher APTT values, indicating that the release of Hep from these samples has favorable anticoagulant property (fig. S21). In addition, hemolysis ratio and the morphology of red blood cells (RBCs) were other important indicators to test the blood compatibility of materials (*29*, *30*). As shown in fig. S21, the hemolysis rates of all samples were less than 5%, and the morphologies of RBCs were normal, indicating that the samples prepared in this work cause little damage to RBCs. The difference in anticoagulant effect between MMNM/Hep and MMNM/Hep/UK may be related to the difference in drug release amount in the first hour. As shown in fig. S22, we tested the amount of Hep released in different samples for the first 1 hour, which showed that MMNM/Hep released approximately 3.1 mg g^{-1} Hep in the first 1 hour, while the release of Hep from MMNM/Hep/UK cannot be detected. The reason may be that the macroporous structure of MMNM/Hep/UK was filled with UK and then the release rate of Hep in the early stage would be slowed to a large extent, so MMNM/Hep showed a faster release rate within the first hour. Further, we also tested the anticoagulant performance of the released Hep solution from MMNM/Hep and MMNM/Hep/UK for 1 hour (fig. S23), which showed that the anticoagulant performance of the released Hep solution from MMNM/Hep was much longer than that from MMNM/Hep/UK, further confirming the above speculation.

Evaluation of thrombolysis in vitro

After determining the release behavior and the blood compatibility of the nanomotors, we then evaluated the thrombolytic ability of the nanomotors in vitro (Fig. 4 and fig. S24). MMNM alone has almost no thrombolytic effect without NIR irradiation, while MMNM after NIR irradiation can reduce the thrombus volume to about 74.7% within 3 hours. Pure NIR irradiation has a small effect on thrombus owing to the temperature change of the solution, and the temperature of MMNM after NIR irradiation can increase to about 42°C (fig. S25), with a photothermal conversion efficiency of about 11.96%, which was beneficial for the thrombolysis. Similarly, we also measured the thrombolytic performance of MMNM/Hep without NIR irradiation, which showed that MMNM/Hep could reduce the thrombus volume to about 75.5% within 3 hours. However, MMN/Hep showed a more obvious thrombolytic effect that the thrombus volume can be reduced to 37.5% after NIR irradiation. There are three possible reasons why MMNM/Hep exhibited better thrombolytic effects under NIR irradiation: (i) The photothermal effect of MMNM under NIR irradiation, (ii) the thrombolytic effect of the Hep, and (iii) the motion effect of MMNM/Hep under NIR irradiation. In addition to being an anticoagulant, Hep also has certain thrombolytic properties (*12*). Meantime, the movement of nanomotors caused by the uneven thermophoresis phenomenon can also promote their penetration into the interior of the thrombus, which is conducive for drugs to perform better thrombolytic effect. As shown in the Fig. 4A, a drug carrier that does not have the ability to move (passive particles) can only stay on the surface of the thrombus and has limited penetration ability, while the nanomotors with movement ability can quickly penetrate into the inside of the thrombus under NIR irradiation.

To explore the thrombolytic ability of samples under different conditions in the simulated vascular system, a dynamic thrombus model consisting of a constant flow pump and a three-dimensional (3D) model of blood vessels was constructed (*31*). Among them, the constant flow pump provided circulating blood flow, and the 3D model of blood vessels was placed and fixed for thrombus. Figure 4B and fig. S26 gave the schematic diagram of the dynamic thrombolytic model and the curve of residual thrombus weight treated with different samples. The residual thrombus weight of thrombus treated with phosphate-buffered saline (PBS) was reduced to 69.0% because of the shearing force of circulating simulated blood on the thrombus (*32*). The thrombolytic effect of the drug-loaded nanomotors under the light condition was obviously better than that under the no-light condition, which is consistent with the trend of static thrombolysis. The percentage of residual thrombus treated by MMNM/Hep/UK/PM was about 37.0%, while MMNM/Hep/UK/PM under NIR irradiation with motion ability can completely dissolve the thrombus

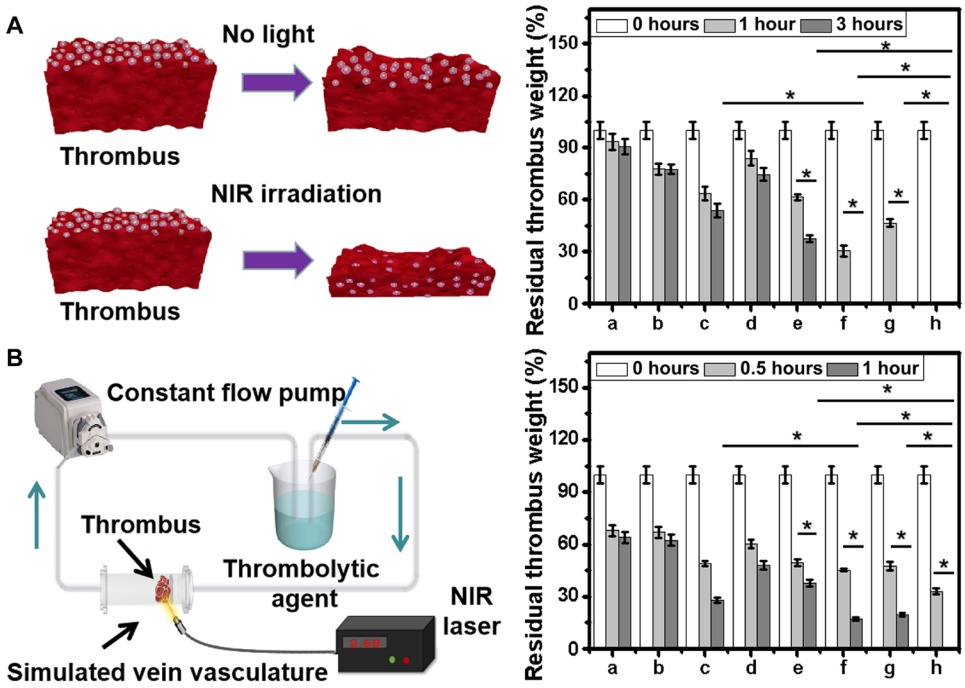

Fig. 4. Thrombolytic effect of the nanomotor in vitro. (**A**) Schematic illustration of static thrombolysis model and the residual thrombus weight in static thrombolysis model. (**B**) Schematic illustration of dynamic thrombolysis model and residual thrombus weight under different conditions (a, phosphate-buffered saline + NIR; b, Hep; c, UK; d, MMNM+NIR; e, MMNM/Hep + NIR; f, MMNM/UK + NIR; g, MMNM/Hep/UK + NIR; and h, MMNM/Hep/UK/PM + NIR). An asterisk denotes statistical significance between bars (*$P < 0.05$) using one-way ANOVA analysis. Experimental data are means ± SD of samples in a representative experiment ($n = 3$).

within 1 hour, which is consistent with the results in static thrombus model.

Evaluation of thrombolysis ability of the nanomotors in vivo

To evaluate the thrombolytic ability of nanomotor in vivo, a rat model with abdominal thrombosis was established (*33*). NIR fluorescent dye Cy5.5 (λ_{ex} 640 nm, λ_{em} 680 nm) was used to detect the targeting ability of the MMNM/PM nanomotors to avoid the influence of autofluorescence of the experimental rat, as illustrated by literatures that light in the region of 650 to 900 nm has deep penetration in tissues and minimal absorption by hemoglobin and water in normal tissues (*34*). To observe the degree of aggregation of materials in the thrombus-vascular site more clearly, we separated the rat thrombus-vascular site during imaging, and the results were shown in Fig. 5A. The MMNM and MMNM/PM nanomotors were stained with Cy5.5 dye to obtain MMNM-Cy5.5 and MMNM/PM-Cy5.5. Results illustrated that Cy5.5 can hardly locate at the thrombus site after being injected into the rats' tail, implying that Cy5.5 displayed no targeting ability to thrombus. A similar phenomenon can be found on MMNM-Cy5.5 without NIR irradiation, while MMNM-Cy5.5 with NIR irradiation showed some fluorescence signals at the thrombus site, indicating that nanomotors with motion ability may enhance their residence ratio at the thrombus site. Meantime, MMNM/PM-Cy5.5 also displayed some fluorescence signals at the thrombus site due to the targeting ability of the PM. The rats treated with MMNM/PM-Cy5.5 with NIR irradiation displayed the strongest fluorescence signal at the site of thrombus, revealing that the synergistic effect of PM and the motion ability of the nanomotor can notably enhance the retention of the nanomotors at the thrombus site. Moreover, to further determine that the nanomotors were located in the blood vessels and thrombus of the rats, we also performed frozen sectioning of the rat blood vessels treated with MMNM/PM-Cy5.5 and observed the existence of the nanomotors in the blood vessels and thrombus. As shown in fig. S27, a large amount of red fluorescence signals (nanomotors) can be found in the blood vessels and thrombus sites, which confirmed that the nanomotors existed at the thrombus and blood vessel sites, further verifying the synergy of the PM and motion ability on targeting effect.

Furthermore, to further quantitatively characterize the ability of the nanomotors to target the blood vessel site of the thrombus, we characterized the material retention efficiency of the thrombus and blood vessel site. First, we freeze-dried and digested the thrombus and blood vessels, then measured the Pt content of the digested solution using the inductively coupled plasma optical emission spectrometry (ICP-OES) method, and lastly calculated the retention efficiency of the samples. When the samples were injected into the body for 24 hours, the retention efficiency of MMNM/PM-Cy5.5 with a targeting effect but no movement ability was about 15%. When NIR irradiation was performed, the retention efficiency can be increased to 26% (fig. S28), which was consistent with the imaging data.

The drug dynamics was conducted in rat for pure drugs and the nanomotors loaded with two drugs (the injected drugs in both cases were the same). It can be seen from fig. S29 that the half-life of pure UK is about 15 min, which was similar with the reported data (10 min) (*35*). In addition, for nanomotors with two kinds of drugs, UK concentrations in rats gradually increased at the beginning 2 hours. After 2 hours, the UK concentration in the rat gradually decreased and then was maintained at a certain level (greater than 40 pg ml^{-1}) in about 4 hours. When it comes to Hep, the highest Hep concentration

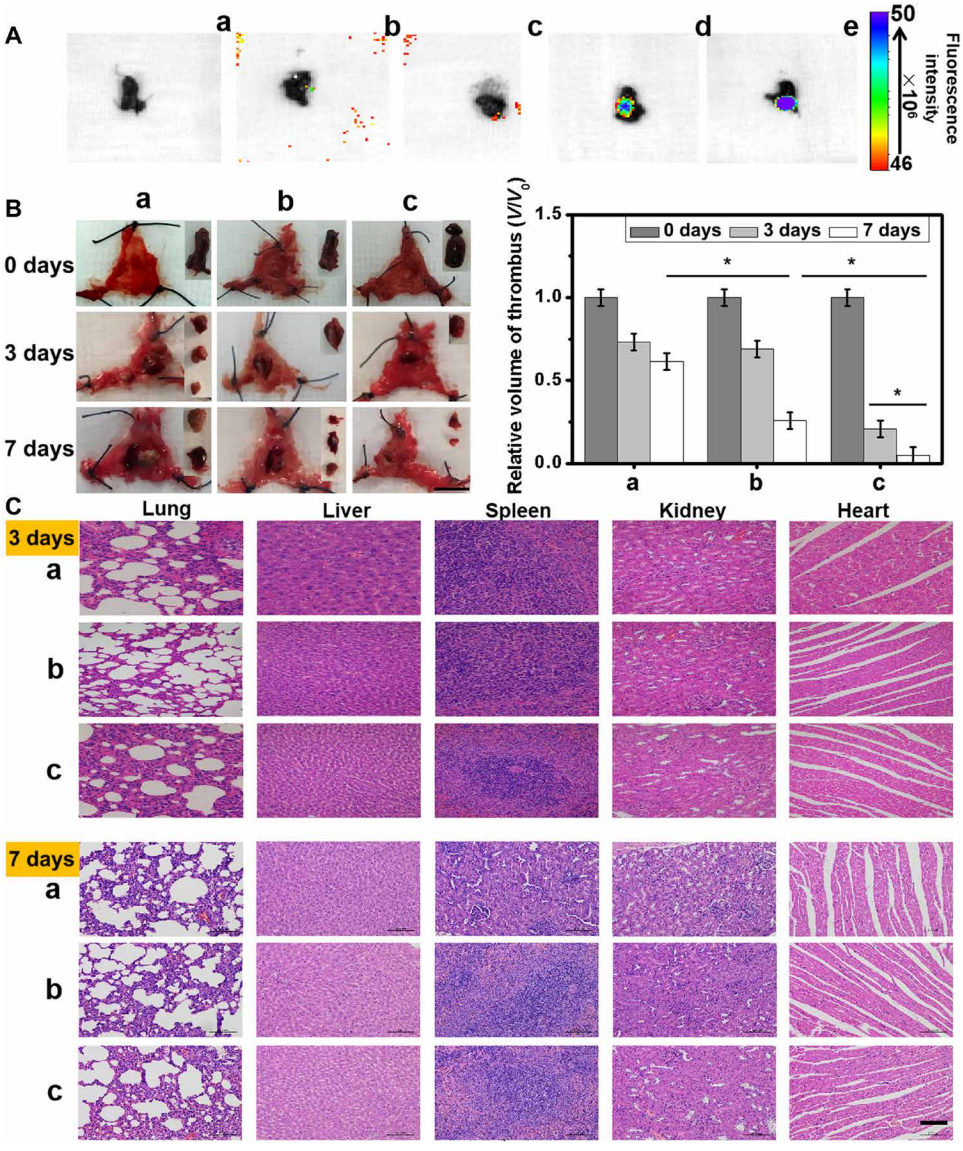

Fig. 5. Thrombolytic effect of the nanomotors in vivo. (**A**) Fluorescence imaging results of the extracted blood vessels with thrombus from rats after being treated with different samples for 24 hours (a, Cy5.5 dye; b, MMNM-Cy5.5; c, MMNM-Cy5.5 + NIR; d, MMNM/PM-Cy5.5; e, MMNM/PM-Cy5.5 + NIR). (**B**) Photographs of blood vessels and thrombus at 0, 3, and 7 days of different samples and corresponding relative volume of thrombus (a, blank; b, UK; c, MMNM/Hep/UK/PM with NIR irradiation; scale bar, 0.5 cm) (Photo credit: Rongliang Wang and Rui Wu, Department of Sports Medicine and Adult Reconstructive Surgery, Nanjing Drum Tower Hospital, The Affiliated Hospital of Nanjing University Medical School, Nanjing 210008, China). (**C**) H&E sections and staining of major organs of rats after 3 and 7 days of thrombolysis. An asterisk denotes statistical significance between bars (*$P < 0.05$) using one-way ANOVA analysis. Experimental data are means ± SD of samples in a representative experiment ($n = 3$) (scale bar, 100 μm).

was found after injection of free Hep, and then its concentration dropped sharply (fig. S30), and its half-life reflected was about 3 to 4 hours, which was close to the value reported in the literature (*36*). For Hep released by nanomotors, the content of Hep could not be detected within the first hour. The possible reason may be that Hep was loaded in the mesoporous core of nanomotors, which was difficult to be detected at the beginning 1 hour. The release of Hep gradually increased from 2 to 48 hours, probably owing to the sustained release of Hep from nanomotors. After 48 hours, the Hep concentration in the rat gradually decreased, but it could still maintain a certain Hep concentration for at least 20 days, displaying that mesoporous structure from the nanomotors can achieve good in vivo Hep slow-release effect for long term.

Then, the thrombolytic effect of the nanomotors in vivo was detected. The photographs of thrombus treated with different samples were shown in Fig. 5B and figs. S31 and S32. It can be seen from figs. S31 and S32 that the relative thrombus volume can be decreased to about 0.56 for MMNM/UK when the treatment time was 3 days, the relative volume of thrombus for MMNM/Hep, MMNM/Hep/UK, and MMNM/Hep/UK/PM were about 0.77, 0.49, and 0.43, respectively. When the treatment time extends to 7 days, MMNM/Hep/UK/PM displayed the best thrombolysis ability among these samples, probably owing to the fact that the targeting ability of PM can promote the aggregation of nanomotors at the thrombus site. The relative volume of thrombus (V/V_0) of the MMNM/Hep/UK/PM nanomotors with NIR irradiation decreases to less than 0.05, implying

good thrombolytic effect of the nanomotors with two-drug release ability and targeting ability.

Last, the biosafety of the samples was assessed. Figure 5C and figs. S33 and S34 displayed the hematoxylin and eosin (H&E) staining results of main organs of the rats treated with different samples for different days, suggesting that the samples did not cause histological toxicity to the main organs of rats. Further, the biodistributions of the nanomotors at 1, 3, and 7 days after injection into rats were investigated in detail. To trace the distribution of the nanomotors in vivo, ICP-OES measurement was used to detect the content of Pt in major organs (liver, spleen, kidneys, heart, and lungs) of rat. As shown in tables S7 and S8, Pt element existed mainly in liver and kidney, demonstrating that the nanomotors may be cleared in metabolic organs (*31*).

The in vivo toxicity of the nanomotors was also detected according to the following procedure. Several rats were intravenously injected with the nanomotors with drugs. These rats were euthanized at 7 and 25 days, and the blood samples were collected for analysis of blood routine and blood serum enzymes. As can be seen in tables S9 to S12, most of the obtained blood parameters were in the normal ranges, indicating that the injected nanomotors will not cause toxicity to the rats during the therapy period and the following days. Meantime, the values of serum enzymes after being treated with nanomotors were also in normal range, indicating low blood toxicity of the nanomotors in vivo.

DISCUSSION

In general, this work constructs a NIR-driven biomimetic targeted nanomotor with a drug-graded release mechanism. A possible motion mechanism was also proposed in this work. The asymmetrically loaded Pt NPs in the MMNM may be regarded as a heating source causing a local temperature gradient around the nanomotors (fig. S35) (*20*). Thus, they display directed motion under the NIR irradiation. Further, to assess the motion behavior of nanomotors in thrombus condition, human fibrinogen was used to construct a thrombus model using thrombin (*12*). To visualize the thrombus and nanomotors, the thrombus was stained with fluorescein isothiocyanate (FITC), and the nanomotors were stained with Cy5.5. As shown in fig. S36, a green fluorescent signal proved that a fluorescently labeled thrombus model was successfully established. According to movie S2 and fig. S36, the nanomotor with red color can move at the green thrombus model, indicating that the nanomotor designed in this work may move at the thrombus site, providing its possibility for deep penetration.

Moreover, it is crucial for the thrombolytic effect that the drug carrier can penetrate into the interior of the thrombus to achieve deep administration. Thus, in this work, the permeation behaviors of the nanomotors at the thrombus site under different conditions (static and dynamic) were studied systematically with qualitative and quantitative investigation. We first studied the penetration behavior of nanomotors under static conditions. The nanomotors were distributed to the thrombus surface under NIR irradiation, then the longitudinal section of the thrombus was fixed and stained, and the existence of nanomotors (black small particles) in the section was observed. As shown in Fig. 6A, under static conditions, the nanomotors cannot move without NIR irridiation, so it can only penetrate by concentration difference, and only a small amount can penetrate into the interior of the thrombus. The penetration depth was approximately 650 μm, while there were almost no MMNM/Hep/UK/PM particles at locations deeper than 650 μm. For nanomotors with mobility after NIR irradiation, not only the amount of penetrated nanomotors was significantly enhanced but also a large number of nanomotors can be found inside the thrombus deeper than 1800 μm. Next, FITC-labeled nanomotors were also used to investigate the permeation behavior in the thrombus under the dynamic thrombus model (Fig. 6B). The FITC-labeled nanomotors (green color) without NIR irradiation had a thrombus distribution depth of less than 1800 μm. For nanomotors under NIR irradiation, green particles can still be observed at a thrombus depth of approximately 4000 μm. In vitro thrombus models under static condition were performed to investigate the location and running trace of motors in the thrombolysis model. The nanomotors stained with Cy5.5 were distributed to the thrombus surface under NIR irradiation for different times, then the longitudinal section of the thrombus was fixed and stained, and the existence of nanomotors (red fluorescence signal) in the section was observed. The depth that the nanomotors can reach in different times was determined by quantitative analysis of the content of nanomotors in the thrombus slice of different depth, so as to judge the relationship between the movement time of nanomotors and the penetration depth. As shown in fig. S37, with the extension of the irradiation time (0 to 8 min), the penetration depth of the nanomotor at the thrombus site gradually increased (200 to 1800 μm), which may provide reference to infer the location and running trace of the nanomotor in vivo.

Further, we also quantitatively characterized the penetration of nanomotors at the thrombus site (static, dynamic, and in vivo condition) and evaluated their infiltration capacity using retention efficiency (residual drug amount*100/given dosage, %). As shown in Fig. 6C, in the static thrombus model, the residual efficiency of MMNM nanomotors in the thrombus was 0.6% without NIR irradiation, which increased to 1.2% with NIR irradiation. While in the dynamic thrombus model (Fig. 6D), the retention ratio of the nanomotors exposed to NIR irradiation was about 10.0%. Both sets of data confirm that the movement of the nanomotor under NIR can effectively increase the residual efficiency of the nanomotor at the thrombus, which may be due to the increased penetration capacity caused by motion of the nanomotors. Moreover, the increase of the residual efficiency under dynamic condition compared with static condition may be attributed to the fact that the shearing force generated by the fluid at the thrombus site can facilitate the nanomotor residual process (*32*).

The above results confirmed that the nanomotors were expected to use their unique motion ability to achieve deep penetration at the thrombus site. It is worth mentioning that the targeting ability of the PM and the motion ability of the NIR-driven nanomotors can greatly increase the retention efficiency of the nanomotors at thrombus (about 26% in vivo, 24 hours; fig. S28), which was much higher than that of the samples without motion ability (about 15%, 24 hours; fig. S28), as well as the untargeted passive drug carrier reported in the literatures (typically lower than 5% and rarely higher than 10%) (*37*, *38*). At the same time, the penetration depth (4000 μm) of the nanomotor in the thrombus site was much higher than that in current literatures (1000 to 2000 μm) (*39*–*41*), which reflects the promoting effect of the movement ability of nanomotors on their penetration performance.

We have also tested whether the nanomotors caused damage to vascular endothelial cells during their motion process. As shown in

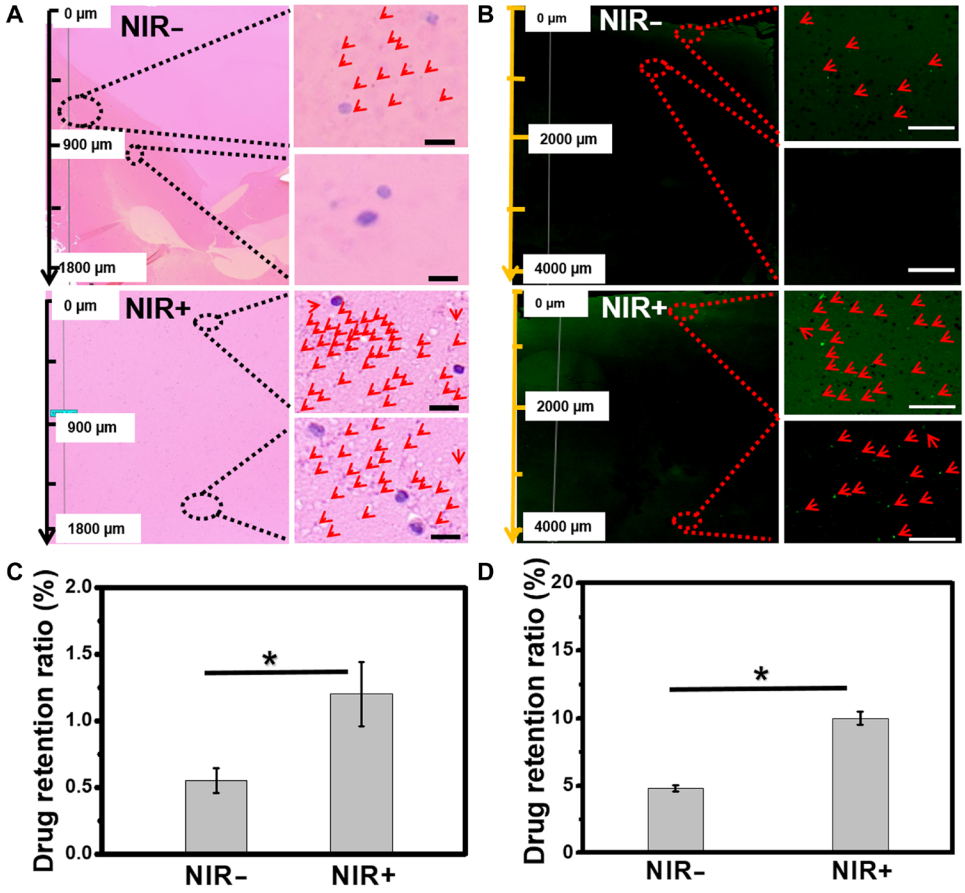

Fig. 6. Thrombotic permeability test of the nanomotors. (**A**) H&E sections and staining of nanomotors penetration into thrombus without and with NIR irradiation under static thrombolysis model (scale bar, 10 μm). (**B**) Frozen section of the nanomotor penetration into thrombus without and with NIR irradiation under a dynamic thrombolysis model (green, the nanomotors) (scale bar, 50 μm). Drug retention ratio without and with NIR irradiation under (**C**) a static thrombolysis model and (**D**) the dynamic thrombolysis model. An asterisk denotes statistical significance between bars (*$P < 0.05$) using one-way ANOVA analysis. Experimental data are means ± SD of samples in a representative experiment ($n = 3$).

fig. S38, the nanomotors caused no damage to human umbilical vein endothelial cells (HUVECs). After incubating the nanomotors under NIR irradiation for 24 hours in HUVECs, the cell viability can still be maintained above 90%, which indicates that the movement of the nanomotors does not cause damage to HUVECs. Meantime, whether the irradiation of NIR and the motion of nanomotors could lead to the blood vessel injury in vivo was also detected. Vascular structure after targeting the thrombus site with the nanomotor for 24 hours was characterized by H&E, elastic fiber staining, reticular fiber staining, and terminal deoxynucleotidyl transferase–mediated deoxyuridine triphosphate nick end labeling (TUNEL) methods (fig. S39). It can be seen clearly that no significant damage to the structure of blood vessels treated by nanomotors, such as elastic plate deformation, detachment of endothelial cells, and inflammatory reaction, indicating that the motion ability of nanomotors will not cause the damage of the blood vessels.

In addition, we also examined the possibility of nanomotors entering from vascular endothelial cells to vascular smooth muscle cells (SMCs). Since the blood vessels contained the endothelial layer and the smooth muscle layer (*42*). If the drug-loading nanomotors can penetrate the endothelial cells and stay in SMCs layer during the therapy time, it is beneficial for the long-term release of Hep by the nanomotors. Therefore, the possibility of nanomotors entering the SMCs from endothelial cells was also investigated. As shown in fig. S40, green fluorescence can be found in the upper HUVECs and weak fluorescent signal in the lower SMCs without NIR irradiation. Under the condition of NIR irradiation, a large amount of green fluorescence signals appeared in the upper layer of HUVECs, indicating that the mobility of the nanomotors also increased the cellular uptake ability, while the SMCs of the lower layer showed more green fluorescence signals. These results implied that the motion ability of the nanomotors can greatly promote the transport process from the endothelial layer to the smooth muscle layer, which was beneficial for the long-term release of anticoagulant drug in the blood vessels.

In summary, we constructed a PM biomimetic modified nanomotors with a drug sequential release mechanism. The purpose of rapid thrombolysis and long-term anticoagulation was achieved by loading different drugs with its unique porous structure. At the same time, the nanomotors can penetrate deeply into the thrombus based on their unique movement ability, thereby improving the therapeutic effect. The experimental results showed that the penetration depth of the nanomotor in thrombus under static conditions can reach more than 1800 μm, and the penetration distance of the

same NP without motion ability was only about 650 μm. Under dynamic conditions, the penetration depth of the nanomotor in the thrombus can be further increased to 4000 μm. Results of animal experiments confirmed that the MMNM/Hep/UK/PM nanomotors had good thrombolytic performance in vivo and can dissolve thrombus volume to less than 5% within 7 days. It is worth mentioning that the motion ability of nanomotors also improves the retention rate in the thrombus. Compared with the NPs without motion ability, the retention rate of nanomotors in the thrombus can be increased from 15 to about 26%. This strategy of using nanomotors to improve drug penetration in thrombus may bring effective ideas for thrombus treatment.

MATERIALS AND METHODS

Materials

Hexadecyl trimethyl ammonium bromide (CTAB), triethanolamine (TEA), cyclohexane, tetraethyl orthosilicate (TEOS), chlorobenzene, H_2PtCl_6, sodium borohydride ($NaBH_4$), isopropanol, toluidine blue, ethanol, and 3-aminopropyltriethoxysilane (APTES) were purchased from Sinopharm Chemical Reagent Co., Ltd. Hep and Cy5.5-NHS were obtained from Aladdin Chemistry Co., Ltd. UK was obtained from Xiamen Huijia Biotechnology Co., Ltd. 3, 3-Dioctadecyloxacarbocyanine perchlorate (DiO; DiOC18), thrombin, human plasma fibrinogen, and FITC were purchased from Shanghai Yuanye Biotechnology Co., Ltd. (China).

Preparation of MMS NPs

MMS NPs were fabricated by a two-step method with a little modification according to previous literatures (*43*). Briefly, 24 ml of CTAB solution (25%, w/w) was treated with ultrasonication to homogeneous solution, followed by adding 36 ml of H_2O. Then, 0.18 g of TEA was added and stirred for 1 hour at 60°C. Sixteen milliliters of cyclohexane and 4 ml of TEOS were carefully injected into above solution and stirred for 24 hours. The obtained sample named as MS NPs was washed by ethanol three times.

Sixty milligrams of MS NPs was dispersed in 6 ml of H_2O, and 0.035 g of TEA was added under an ultrasonic condition and maintained for 15 min. Then, 4 ml of CTAB solution (25%, w/w) was added and stirred for 1 hour at 60°C. Next, 8.75 ml of chlorobenzene and 0.82 ml of TEOS were added and stirred continuously for 12 hours. The obtained sample named as MMS NPs were collected by centrifugation at 10,000 rpm for 5 min. Further, the MMS NPs were calcined at 550°C for 5 hours to remove the template CTAB.

Preparation of MMNM nanomotors

Twenty milligrams of MMS was fully dispersed in 0.6 ml of isopropanol followed by adding of 0.53 ml of H_2PtCl_6 solution (0.019 M) and then stirred for 6 hours at room temperature. After vacuum drying, the products were redispersed in the mixture with 0.6 ml of isopropyl alcohol and 0.2 ml of ethanol with the addition of $NaBH_4$ (0.001 g). After further stirring for 4 hours, the products named as MMNM were obtained by centrifugation and drying in a vacuum oven.

The obtained MMNM nanomotors (20 mg) were then suspended in 40 ml of EtOH: APTES mixture (20:1, v/v) and stirred for 24 hours. In addition, MMNM nanomotors with amine modification (named as MMNM-NH_2) were collected by centrifugation (4000 rpm, 10 min).

In addition, the preparation of MMNM-FITC was as follows: 30 mg of MMNM was dispersed in 30 ml of ethanol and 30 ml of water. Then, 100 μl of APTES and 400 μl of FITC solution (0.25 mg ml^{-1}) were added at 40°C and stirred for 24 hours. After centrifugation with water and ethanol three times each, the obtained product was named as MMNM-FITC.

The preparation of MMNM-Cy5.5 was as follows: 50 mg of MMNM-NH_2 was dispersed in 10 ml of $NaHCO_3$ solution (0.1 M), and 1.25 ml of Cy5.5-NHS solution [1 mg ml^{-1}, in dimethyl sulfoxide (DMSO)] was added for overnight in the dark. Then, the obtained product was dialyzed for 48 hours to remove the excess DMSO. Last, the product named as MMNM-Cy5.5 was obtained by freeze drying.

Preparation and characterization of MMNM/PM nanomotors

In brief, 10 ml of blood samples was centrifuged at 1500 rpm for 15 min. Then, the upper serum was carefully taken out and further centrifuged at 3000 rpm for 15 min. The obtained precipitation was repeatedly frozen and thawed eight times between room temperature and −80°C and then centrifuged by 10,000 rpm to obtain PM.

Two hundred microliters of PM was added to 2 ml of MMNM (1 mg ml^{-1}) with ultrasonic treatment for 10 min, and the obtained product was named as MMNM/PM. To confirm the presence of PM from MMNM/PM nanomotors, MMNM-Cy5.5/PM nanomotors were stained with DiO (10 μM) for 20 min. Fluorescence microscopy images were obtained using CLSM (HP Apo TIRF 100X N.A. 1.49, Nikon, Ti-E-A1R, Japan) with and 100× microscope objectives under green light (488 nm) and red light (647 nm).

Besides, we used Western blot analysis to assess the existence of GPIIb-IIIa complex from the MMNM/PM. First, 500 μl of protein lysis buffer radio immunoprecipitation assay [which was brought to 1 mM phenylmethanesulfonyl fluoride (PMSF) by adding 100 mM PMSF stock] was added to separated platelets or MMNM/PM nanomotors solution, which were centrifuged at 12,000 rpm for 15 min at 4°C. The total protein concentration was determined by a bicinchoninic acid (BCA) method using the Pierce BCA Protein Assay Kit (Thermo Fisher Scientific, Lithuania). Second, the equal quantities of the total protein (30 μg) of cellular lysate protein were subjected to 12% SDS–polyacrylamide gel electrophoresis and transferred onto polyvinylidene fluoride (PVDF) membranes. The PVDF membranes were blocked for 2 hours at room temperature using 4% nonfat milk–tris-buffered saline with Tween (TBST) solution. The PVDF membranes were incubated with primary antibodies, anti-GPIIIa (ProteinTech Group, Chicago, IL, USA), anti-GPIIb (ProteinTech Group, Chicago, IL, USA), and anti–β-actin (Cell Signaling Technology Inc., MA, USA) at 4°C overnight (the respective dilutions were 1:1000, 1:1000, and 1:5000). Following successive washes, the PVDF membranes were incubated with goat anti-rabbit horseradish peroxidase–labeled secondary antibodies (Fude Biological Technology Co., Hangzhou, China) for 2 hours at room temperature. Last, the signals were revealed by using a Tanon 5200 system (Bio Tanon, Shanghai, China).

Analysis of nanomotors' motion

Aqueous solution of nanomotors was placed on a glass slide. An inverted optical microscope (Nanjing Jiangnan Yongxin Optics Co., Ltd., XD-202) with a 40× water objective was used for video capture of the nanomotor movement. NIR light (808 nm with different power density) was applied as the propulsion source. The providing particle trajectory analysis was conducted by Software of ImageJ.

To further observe the movement of the nanomotor at the thrombus site, we established a thrombus model according to the

previously published literature (*12*). The human plasma fibrinogen (1 mg ml^{-1}) as a source of thrombus was dissolved in 50 mM tris-HCl and 140 mM NaCl. Then, 2.5 mM $CaCl_2$ and 10 μl of FITC were added and incubated at 50°C for 2 hours. CLSM was used to observe and record the motion behavior of the nanomotor in the fluorescent thrombus model.

Drug loading and releasing in vitro

Ten milligrams of samples was suspended in Hep solution (2 mg ml^{-1} in PBS) and incubated for 24 hours at room temperature. Then, a Hep-loaded sample (MMNM/Hep) was collected with centrifugation (10,000 rpm, 10 min) by washing with PBS three times to ensure complete removal of nonloaded Hep. The MMNM/Hep was redistributed in UK solution (0.25 mg ml^{-1}, 2 ml in PBS) for 24 hours at room temperature. The UK-loaded MMNM/Hep (MMNM/Hep/UK) was then collected by centrifugation (10,000 rpm, 10 min). The preparation process of MMNM/Hep and MMNM/UK was similar to the above procedure.

To test the in vitro release of Hep and UK from the nanomotors, MMNM/Hep/UK/PM nanomotors (20 mg) were dispersed in PBS (pH = 7.35 to 7.45, 4 ml) at 37°C on an orbital shaker. The released drug solution was collected at a certain time by centrifugation. Three milliliters of the supernatant was taken for each centrifugation (10,000 rpm, 10 min) and then replenished with PBS solution (3 ml). The release behavior of MMNM/Hep/UK/PM nanomotors under NIR irradiation was performed by NIR irradiation for 10 min (2.5 W cm^{-2}) at the beginning of the release process. The released amount of Hep was determined using the toluidine blue method: A standard solution of Hep with the concentration of 1 mg ml^{-1} was prepared. Then, the toluidine blue solution (0.005%, 500 ml) containing HCl (2 M, 2.5 ml) and NaCl (1 g) was prepared. Standard Hep dilutions with concentrations of 0.5 to 14 μg ml^{-1} were used to obtain the standard curve. For the Hep test, toluidine blue solution (2.5 ml) and Hep solution (2.5 ml) were mixed together, which was shaken vigorously for 30 s. Five milliliters of hexane was added to extract the colored substance, and the absorbance was detected at 620 nm using the visible-light spectrophotometer. The release of UK was determined using a UK kit (Jiangsu Meimian Industrial Co., Ltd.). The drug release profiles of Hep or UK from MMNM/Hep and MMNM/UK were also detected according to the above procedure.

Coagulation time assays in vitro

Plasma was obtained by centrifugation of fresh rabbit blood at 2500 rpm for 15 min. Then, the different samples (0.l ml, 1 mg ml^{-1}) or the drug release solution (0.l ml) was cultured with plasma for 1 hour at 37°C (PBS as the blank group). The coagulation time of the samples was tested by a semiautomated coagulometer (RT-2204C, Rayto, USA).

Hemolysis and morphological changes of RBCs

For hemolysis test, RBCs were collected from fresh blood by centrifuging at 1500 rpm for 10 min and then were diluted with PBS to a 2% cell suspension. Samples (2.5 ml) in PBS were incubated with 2% dilute RBC suspensions in PBS at 37°C for 30 min. The mixture consisting of 2.5 ml of water and 2.5 ml of 2% RBC diluent was the positive control, and the mixture consisting of 2.5 ml of PBS and 2.5 ml of 2% RBC diluent was the negative control. Negative and positive control groups were incubated at the same time. Then, the solution was centrifuged at 2500 rpm for 5 min to take out the supernatant to be detected by using a microplate reader (540 nm; Bio-Rad Co., Ltd., USA). The calculation formula of hemolysis rate is as follows: Hemolysis (%) = (sample − negative)/(positive − negative) × 100%.

For the observation of RBCs morphology, the different solutions mentioned above after incubation were dripped onto the slide for observation. The morphology of RBCs treated with the samples was observed with an optical microscope (Olympus BX41) and a camera (Olympus E-620).

Preparation of artificial thrombus

The artificial thrombus for static thrombolysis assessment was prepared according to a published report (*44*). Fresh blood was collected and divided into a number of tubes with equal volumes. Each tube was mixed with thrombin (500 U ml^{-1}) and placed into a drying oven at 37°C for 3 hours. Then, the tubes were transferred to 4°C for another 3 days, and the artificial thrombus was formed. The artificial thrombus for dynamic thrombolysis assessment was prepared by heating gelatin (0.05 g) and blood (3 ml) at 80°C for 1 hour, then cooled to room temperature and stored at 4°C.

Thrombolysis evaluation in vitro

Static thrombolysis assessment

The prepared thrombus was placed into a tube containing 1 ml of different sample solutions (0.4 mg ml^{-1}). Then, the bottles were placed at 37°C, and the thrombus was taken out to be weighed and photographed at a setting time. Among them, the NIR irradiation group was required to perform NIR irradiation for 10 min. The wavelength of NIR laser was 808 nm, the power density was 2.5 W cm^{-2}, and the irradiation time was 10 min.

Dynamic thrombolysis assessment

The simulated vein vasculature model was chosen to further study thrombolysis. Different-samples solutions (0.4 mg ml^{-1}) were added into the simulation of blood vessels, and the prepared thrombus was placed at designed site. The weight of thrombus under different conditions was recorded at the setting time. Among them, the NIR irradiation group was required to perform NIR irradiation for 10 min.

Photothermal test in vitro

The solutions of PBS and MMNM (0.4 mg ml^{-1}) were irradiated for 10 min with NIR laser (2.5 W cm^{-2}). At the same time, the temperature of the solution was recorded every 30 s with a thermal imager (FOTRIC 226S-L28).

Thrombus-targeted evaluation in vivo

Following previous literature (*33*), we established a rat model with celiac vein thrombus. Then, the treated rats were randomly divided into five groups and intravenously injected with different samples (Cy5.5, MMNM-Cy5.5, MMNM-Cy5.5 + NIR, MMNM/PM-Cy5.5, MMNM/PM-Cy5.5 + NIR, 0.4 mg ml^{-1}, 0.2 ml). Among them, the NIR irradiation group was required to perform NIR irradiation for 10 min. The blood vessels and thrombus of rat were carefully removed for imaging, frozen sections, and ICP-OES measurement after 24 hours.

Pharmacokinetic test

Rats were randomly divided into two groups (n = 6). Before the injection of drugs, 1 ml of blood was taken from each rat through its eyeball and then followed by injection of different samples (the mixture of UK and Hep, nanomotors with two drugs). Then, blood was taken from each group at each set time point for 20 days. The

obtained fresh blood was immediately centrifuged to obtain the supernatant serum, which was detected with the UK assay kit and the Hep assay kit, respectively.

Thrombolysis and biosafety assessment in vivo

The study was carried out in strict accordance with the recommendations in the Guide for Care and Use of Laboratory Animals of the National Institutes of Health. All animal care and experiments were carried out in accordance with the guidelines and were approved by the Ethics Committee of Drum Tower Hospital, Medical School of Nanjing University, China. The rats were intravenously injected every day with different samples for 3 and 7 days, respectively. Among them, the NIR irradiation group was required to perform NIR irradiation (2.5 W cm^{-2}) for 10 min every day after injection of nanomotors. The blood vessels and thrombus were taken out and photographed, and the major organs of rats were separated. The Pt amount of the major organs was quantified by ICP-OES and qualified by H&E staining. In addition, to further observe the damage of blood vessels, H&E staining, elastic fiber staining, reticular fiber staining, and TUNEL staining were used for staining the blood vessels of rats treated with the PBS group and the nanomoter group, respectively.

MTT assay

The HUVECs were seeded in 96-well plates at a density of 5×10^4 cells ml^{-1}. The cells were cocultured with different samples without or with NIR irradiation (10 min) for 24 hours. Then, MTT (3-(4,5-dimethylthiazol-2-yl)-2,5- diphenyltetrazolium bromide) reagent (50 μl, 5 mg ml^{-1}) was added to each well. After coculture of MTT with cells for another 4 hours, the produced formazan precipitates were dissolved in DMSO, and the absorbance was tested with a microplate reader (490 nm).

Thrombotic permeability test

Static thrombotic penetration

The freshly prepared thrombus was randomly divided into two groups and placed in 1 ml of MMNM nanomotor solution (0.4 mg ml^{-1}). The above solutions were treated with and without NIR for 10 min, respectively. Then, the thrombus was taken out and subjected to H&E staining and ICP-OES to measure the penetration depth and the residual mass of different samples in the thrombus.

Dynamic thrombotic penetration

One milliliter of MMNM-FITC solution (0.4 mg ml^{-1}) was added into the simulation of blood vessels in the simulated vein vasculature model. After being treated with or without NIR irradiation (2.5 W cm^{-2}) for 10 min, respectively, the thrombus was taken out and subjected to frozen sections and ICP-OES measurement to detect the penetration depth and the residual mass of different samples in the thrombus.

Penetration behavior investigation

To investigate the permeability of the nanomotor from HUVECs to SMCs, the above cells (the cell density of 5×10^5 cell ml^{-1}) were added into the glass slide, respectively. After overnight incubation, MMNM-FITC nanomotors (0.4 mg ml^{-1}) were added to the glass slide of HUVECs with NIR irradiation for 10 min, followed by incubation for 2 hours. The above glass slide was carefully removed and then placed with the glass slide of SMCs and cultured for 12 hours. The medium was replaced with fresh medium, and then the cell nuclei were stained with 4′,6-diamidino-2-phenylindole. Images were taken using CLSM.

Statistical analysis

The statistical analysis was conducted by a one-way analysis of variance (ANOVA) with the Bonferroni post hoc test or Tamhane's T2 post hoc test with the use of SPSS software (version 19.0). An asterisk denotes statistical significance between bars ($*P < 0.05$).

SUPPLEMENTARY MATERIALS

Supplementary material for this article is available at http://advances.sciencemag.org/cgi/content/full/6/22/eaaz9014/DC1

View/request a protocol for this paper from *Bio-protocol*.

REFERENCES AND NOTES

1. A. S. Go, D. Mozaffarian, V. L. Roger, E. J. Benjamin, J. D. Berry, M. J. Blaha, S. Dai, E. S. Ford, C. S. Fox, S. Franco, H. J. Fullerton, C. Gillespie, S. M. Hailpern, J. A. Heit, V. J. Howard, M. D. Huffman, S. E. Judd, B. M. Kissela, S. J. Kittner, D. T. Lackland, J. H. Lichtman, L. D. Lisabeth, R. H. Mackey, D. J. Magid, G. M. Marcus, A. Marelli, D. B. Matchar, D. K. McGuire, E. R. Mohler, C. S. Moy, M. E. Mussolino, R. W. Neumar, G. Nichol, D. K. Pandey, N. P. Paynter, M. J. Reeves, P. D. Sorlie, J. Stein, A. Towfighi, T. N. Turan, S. S. Virani, N. D. Wong, D. Woo, M. B. Turner; American Heart Association Statistics Committee and Stroke Statistics Subcommittee, Executive summary: Heart disease and stroke statistics-2014 update a report from the american heart association. *Circulation* **129**, 399–410 (2014).
2. J. A. Heit, F. A. Spencer, R. H. White, The epidemiology of venous thromboembolism. *J. Thromb. Thrombolysis* **41**, 3–14 (2016).
3. J. A. Heit, Epidemiology of venous thromboembolism. *Nat. Rev. Cardiol.* **12**, 464–474 (2015).
4. R. Lecumberri, A. Alfonso, D. Jimenez, C. Fernandez Capitan, P. Prandoni, P. S. Wells, G. Vidal, G. Barillari, M. Monreal; RIETE investigators, Dynamics of case-fatalilty rates of recurrent thromboembolism and major bleeding in patients treated for venous thromboembolism. *Thromb. Haemost.* **110**, 834–843 (2013).
5. G. W. Landman, R. O. Gans, Oral rivaroxaban for symptomatic venous thromboembolism. *N. Engl. J. Med.* **364**, 1178 (2011).
6. R. S. Marshall, Progress in intravenous thrombolytic therapy for acute stroke. *JAMA Neurol.* **72**, 928–934 (2015).
7. M. Juenet, R. Aid-Launais, B. Li, A. Berger, J. Aerts, V. Ollivier, A. Nicoletti, D. Letourneur, C. Chauvierre, Thrombolytic therapy based on fucoidan-functionalized polymer nanoparticles targeting P-selectin. *Biomaterials* **156**, 204–216 (2018).
8. H. Kobayashi, R. Watanabe, P. L. Choyke, Improving conventional enhanced permeability and retention (EPR) effects; what is the appropriate target? *Theranostics* **4**, 81–89 (2013).
9. Z. J. Chen, T. Xia, Z. L. Zhang, S. Z. Xie, T. Wang, X. H. Li, Enzyme-powered Janus nanomotors launched from intratumoral depots to address drug delivery barriers. *Chem. Eng. J.* **375**, 122109 (2019).
10. X. Ma, S. Jang, M. N. Popescu, W. E. Uspal, A. Miguel-López, K. Hahn, D.-P. Kim, S. Sánchez, Reversed Janus micro/nanomotors with internal chemical engine. *ACS Nano* **10**, 8751–8759 (2016).
11. M. Xuan, Z. Wu, J. Shao, L. Dai, T. Si, Q. He, Near infrared light-powered Janus mesoporous silica nanoparticle motors. *J. Am. Chem. Soc.* **138**, 6492–6497 (2016).
12. J. Shao, M. Abdelghani, G. Shen, S. Cao, D. S. Williams, J. C. M. van Hest, Erythrocyte membrane modified Janus polymeric motors for thrombus therapy. *ACS Nano* **12**, 4877–4885 (2018).
13. EINSTEIN Investigators, R. Bauersachs, S. D. Berkowitz, B. Brenner, H. R. Buller, H. Decousus, A. S. Gallus, A. W. Lensing, F. Misselwitz, M. H. Prins, G. E. Raskob, A. Segers, P. Verhamme, P. Wells, G. Agnelli, H. Bounameaux, A. Cohen, B. L. Davidson, F. Piovella, S. Schellong, Oral rivaroxaban for symptomatic venous thromboembolism. *N. Engl. J. Med.* **363**, 2499–2510 (2010).
14. B. A. Hutten, M. H. Prins, Duration of treatment with vitamin K antagonists in symptomatic venous thromboembolism. *Cochrane Database Syst. Rev.* **1**, CD001367 (2006).
15. Y. X. Yang, J. B. Zhang, W. M. Yang, J. D. Wu, R. S. Chen, Adsorption properties for urokinase on local diatomite surface. *Appl. Surf. Sci.* **206**, 20–28 (2003).
16. B. Mulloy, S. Khan, S. J. Perkins, Molecular architecture of heparin and heparan sulfate: Recent developments in solution structural studies. *Pure Appl. Chem.* **84**, 65–76 (2012).
17. Z. W. Chen, Q. Y. Hu, Z. Gu, Leveraging engineering of cells for drug delivery. *Acc. Chem. Res.* **51**, 668–677 (2018).
18. Y. F. Lu, Q. Y. Hu, C. Jiang, Z. Gu, Platelet for drug delivery. *Curr. Opin. Biotechnol.* **58**, 81–91 (2019).
19. Q. Y. Hu, C. G. Qian, W. J. Sun, J. Q. Wang, Z. W. Chen, H. N. Bomba, H. L. Xin, Q. D. Shen, Z. Gu, Engineered nanoplatelets for enhanced treatment of multiple myeloma and thrombus. *Adv. Mater.* **28**, 9573–9580 (2016).

20. Z. G. Wu, X. K. Lin, Y. J. Wu, T. Y. Si, J. M. Sun, Q. He, Near-infrared light-triggered "on/off" motion of polymer multilayer rockets. *ACS Nano* **8**, 6097–6105 (2014).
21. N. Zhang, M. H. Li, X. T. Sun, H. Z. Jia, W. G. Liu, NIR-responsive cancer cytomembrane-cloaked carrier-free nanosystems for highly efficient and self-targeted tumor drug delivery. *Biomaterials* **159**, 25–36 (2018).
22. J. P. Xu, X. Q. Wang, H. Y. Yin, X. Cao, Q. Y. Hu, W. Lv, Q. W. Xu, Z. Gu, H. L. Xin, Sequentially site-specific delivery of thrombolytics and neuroprotectant for enhanced treatment of ischemic stroke. *ACS Nano* **13**, 8577–8588 (2019).
23. Q. Y. Hu, W. J. Sun, C. G. Qian, C. Wang, H. N. Bomba, Z. Gu, Anticancer platelet-mimicking manovehicles. *Adv. Mater.* **27**, 7043–7050 (2015).
24. M. J. Xuan, R. Mestre, C. Y. Gao, C. Zhou, Q. He, S. Sánchez, Noncontinuous super-diffusive dynamics of a light-activated nanobottle motor. *Angew. Chem. Int. Ed.* **57**, 6838–6842 (2018).
25. Q. Wang, S. L. Hu, Y. B. Wu, Q. Niu, Y. Y. Huang, F. Wu, X. T. Zhu, J. Fan, G. Y. Yin, M. M. Wan, C. Mao, M. Zhou, Multiple drug delivery from mesoporous coating realizing combination therapy for bare metal stents. *Langmuir* **35**, 3126–3133 (2019).
26. R. F. Luo, J. Zhang, W. H. Zhuang, L. Deng, L. H. Li, H. C. Yu, J. Wang, N. Huang, Y. B. Wang, Multifunctional coatings that mimic the endothelium: surface bound active heparin nanoparticles with in situ generation of nitric oxide from nitrosothiols. *J. Mater. Chem. B* **6**, 5582–5595 (2018).
27. V. Dubovoy, A. Ganti, T. Zhang, H. Al-Tameemi, J. D. Cerezo, J. M. Boyd, T. Asefa, One-pot hydrothermal synthesis of benzalkonium-templated mesostructured silica antibacterial agents. *J. Am. Chem. Soc.* **140**, 13534–13537 (2018).
28. H. P. Sun, J. H. Su, Q. S. Meng, Q. Yin, L. L. Chen, W. W. Gu, Z. W. Zhang, H. J. Yu, P. C. Zhang, S. L. Wang, Y. P. Li, Cancer cell membrane coated gold nanocages with hyperthermia-triggered drug release and homotypic target inhibit growth and metastasis of breast cancer. *Adv. Funct. Mater.* **27**, 1604300 (2017).
29. J. Shi, M. Y. Wang, Z. Sun, Y. Y. Liu, J. N. Guo, H. L. Mao, F. Yan, Aggregation-induced emission-based ionic liquids for bacterial killing, imaging, cell labeling, and bacterial detection in blood cells. *Acta Biomater.* **97**, 247–259 (2019).
30. H. Chen, X. B. Wang, Q. Zhou, P. Xu, Y. Liu, M. Wan, M. Zhou, C. Mao, Preparation of vascular endothelial cadherin loaded-amphoteric copolymer decorated coronary stents for anticoagulation and endothelialization. *Langmuir* **33**, 13430–13437 (2017).
31. X. L. Wang, C. C. Wei, M. K. Liu, T. Yang, W. M. Zhou, Y. Liu, K. Hong, S. H. Wang, H. B. Xin, X. W. Ding, Near-infrared triggered release of uPA from nanospheres for localized hyperthermia-enhanced thrombolysis. *Adv. Funct. Mater.* **27**, 1701824 (2017).
32. N. Korin, M. Kanapathipillai, B. D. Matthews, M. Crescente, A. Brill, T. Mammoto, K. Ghosh, S. Jurek, S. A. Bencherif, D. Bhatta, A. U. Coskun, C. L. Feldman, D. D. Wagner, D. E. Ingber, Shear-activated nanotherapeutics for drug targeting to obstructed blood vessels. *Science* **337**, 738–742 (2012).
33. J. A. Diaz, A. T. Obi, D. D. Myers, J. S. K. Wrobleski, P. K. Henke, N. Mackman, T. W. Wakefield, Critical review of mouse models of venous thrombosis. *Arterioscler. Thromb. Vasc. Biol.* **32**, 556–562 (2012).
34. Z. X. Lu, F. Y. Huang, R. Cao, G. H. Tan, G. H. Yi, N. Y. He, L. F. Xu, L. M. Zhang, Intrinsic, cancer cell-selective toxicity of organic photothermal nanoagent: a simple formulation for combined photothermal chemotherapy of cancer. *ACS Appl. Mater. Interfaces* **10**, 26028–26038 (2018).
35. S. Koudelka, R. Mikulik, J. Mašek, M. Raška, P. T. Knotigová, A. D. Miller, J. Turánek, Liposomal nanocarriers for plasminogen activators. *J. Control. Release* **227**, 45–57 (2016).
36. J. Martínez-González, L. Vila, C. Rodríguez, Bemiparin: second-generation, low-molecular-weight heparin for treatment and prophylaxis of venous thromboembolism. *Expert. Rev. Cardiovasc. Ther.* **6**, 793–802 (2008).
37. F. Peng, Y. J. Men, Y. F. Tu, Y. M. Chen, D. A. Wilson, Nanomotor-based strategy for enhanced penetration across vasculature model. *Adv. Funct. Mater.* **28**, 1706117 (2018).
38. M. Luo, Y. Z. Feng, T. W. Wang, J. G. Guan, Micro-/Nanorobots at work in active drug delivery. *Adv. Funct. Mater.* **28**, 1706100 (2018).
39. T. W. Chung, S. S. Wang, W. J. Tsai, Accelerating thrombolysis with chitosan-coated plasminogen activators encapsulated in poly-(lactide-co-glycolide) (PLGA) nanoparticles. *Biomaterials* **29**, 228–237 (2008).
40. J. Xu, J. Zhou, Y. X. Zhong, Y. Zhang, J. Liu, Y. L. Chen, L. M. Deng, D. L. Sheng, Z. G. Wang, H. T. Ran, D. J. Guo, Phase transition nanoparticles as multimodality contrast agents for the detection of thrombi and for targeting thrombolysis: *in vitro* and *in vivo* experiments. *ACS Appl. Mater. Interfaces* **9**, 42525–42535 (2017).
41. A. S. Wolberg, Thrombin generation and fibrin clot structure. *Blood Rev.* **21**, 131–142 (2007).
42. M. H. Kural, J. Wang, L. Q. Gui, Y. F. Yuan, G. X. Li, K. L. Leiby, E. Quijano, G. Tellides, W. M. Saltzman, L. E. Niklason, Fas ligand and nitric oxide combination to control smooth muscle growth while sparing endothelium. *Biomaterials* **212**, 28–38 (2019).
43. P. L. Abbaraju, A. K. Mek, H. Song, Y. N. Yang, M. Jambhrunkar, J. Zhang, C. Xu, M. H. Yu, C. Z. Yu, Asymmetric silica nanoparticles with tunable head-tail structures enhance hemocompatibility and maturation of immune cells. *J. Am. Chem. Soc.* **139**, 6321–6328 (2017).
44. T. Yang, X. Ding, L. Dong, C. Hong, J. Ye, Y. Xiao, X. Wang, H. Xin, Platelet-mimic uPA delivery nanovectors based on Au rods for thrombus targeting and treatment. *ACS Biomater Sci. Eng.* **4**, 4219–4224 (2018).
45. Y. L. Liu, K. L. Ai, J. H. Liu, M. Deng, Y. Y. He, L. H. Lu, Dopamine-melanin colloidal nanospheres: an efficient near-infrared photothermal therapeutic agent for in vivo cancer therapy. *Adv. Mater.* **25**, 1353–1359 (2013).
46. W. Z. Ren, Y. Yan, L. Y. Zeng, Z. Z. Shi, A. Gong, P. Schaaf, D. Wang, J. S. Zhao, B. B. Zou, H. S. Yu, G. Chen, E. M. B. Brown, A. G. Wu, A near infrared light triggered hydrogenated black TiO_2 for cancer photothermal therapy. *Adv. Healthc. Mater.* **4**, 1526–1536 (2015).

Acknowledgments

Funding: The work was supported by Jiangsu Collaborative Innovation Center of Biomedical Functional Materials, social development project of Jiangsu Natural Science Foundation (no. BE2019744), National Natural Science Foundation of China (21603105, 21571104), Jiangsu Key Technology RD Program (BE2016010, BE2015603), Technology Support Program of Science and Technology Department of Jiangsu Province (BE2015703), Huaian Biofunctional Materials and Analysis Technology Innovation Platform (HAP201612), the Excellent Young Scholars NSFC (81622033), National Science Foundation of China (81572129), Social Development Project of Jiangsu Provincial Science and Technology Department (BE2016609), Jiangsu Provincial Key Medical Talent Foundation, and Six Talent Peaks Project of Jiangsu Province (WSW-061). **Author contributions:** C.M., D.S., and M.W. designed experiments and analyzed the data. Q.W., Y.Y., L.F., X.W., Y.Z., Z.M., B.Z., F.W., D.F., Y.H., and T.L. performed experiments. Q.J., X.X., R.Wa, and R.Wu. conducted the animal experiments. M.W. and Q.W. wrote the manuscript. C.M. and D.S. oversaw the work. **Competing interests:** The authors declare that they have no competing interests. **Data and materials availability:** All data needed to evaluate the conclusions in the paper are present in the paper and/or the Supplementary Materials. Additional data related to this paper may be requested from the authors.

Submitted 18 October 2019
Accepted 18 March 2020
Published 27 May 2020
10.1126/sciadv.aaz9014

Citation: M. Wan, Q. Wang, R. Wang, R. Wu, T. Li, D. Fang, Y. Huang, Y. Yu, L. Fang, X. Wang, Y. Zhang, Z. Miao, B. Zhao, F. Wang, C. Mao, Q. Jiang, X. Xu, D. Shi, Platelet-derived porous nanomotor for thrombus therapy. *Sci. Adv.* **6**, eaaz9014 (2020).